

ORIGINAL ARTICLE

Monitoring of Ti-25Nb and Ti-25Nb-1O shape memory alloys in the initial stage of tensile deformation by combined techniques of acoustic emission and digital image correlation

Karol Marek Golasiński  · Adam Brodecki · Zbigniew Ranachowski · Wataru Tasaki · Elżbieta Alicja Pieczyska · Hee Young Kim

Received: 25 March 2025 / Revised: 7 November 2025 / Accepted: 23 November 2025

© The Author(s) 2025

Abstract

This work concerns an experimental investigation of the Ti-25Nb and Ti-25Nb-1O (at%) SMAs in the initial stage of tensile deformation using acoustic emission (AE) and digital image correlation (DIC). The stress-strain responses of the considered SMAs are different. The Ti-25Nb SMA exhibits shape memory effect due to the stress-induced martensitic transformation from the cubic β phase to the orthorhombic α'' phase. In the case of the Ti-25Nb-1O SMA, the addition of 1 at% of oxygen results in a nonlinear superelastic behavior with small hysteresis and an increased yield stress. The stress-induced phase transformation in the Ti-25Nb-1O SMA is hindered due to the addition of oxygen interstitials. The difference between the deformation mechanisms and the resulting mechanical behaviors of the SMAs was clearly reflected by the recorded AE signals and deformation fields. It was shown that the AE can serve to track the development of the stress-induced phase transformations in the Ti-25Nb and Ti-25Nb-1O SMAs during tension. The AE signals were correlated to the strain fields of the SMAs, which showed a Lüders-type deformation of the Ti-25Nb SMA and a distinct but still inhomogeneous deformation of the Ti-25Nb-1O SMA. The results of this study show that DIC and AE techniques are effective tools for monitoring phase transformations of the Ti-25Nb and Ti-25Nb-1O SMAs during tensile loading.

Keywords Shape memory alloys · Oxygen interstitials · Martensitic transformation · Acoustic emission · Digital image correlation

1 Introduction

Tensile tests supported by means of special monitoring techniques can contribute to deepen the knowledge about the kinetics of the deformation mechanisms of the tested materials. In particular, acoustic emission (AE) is a nondestructive technique that is very sensitive to the changes related to microscopic processes occurring in a considered material when it is subjected to an external load [1]. AE signal is generated by the rapid release of energy



from a localized source within a material in a form of elastic waves. The AE signals can serve to identify the locations and activity levels of the sources such as the motion of dislocations or twin formation, the development of cracks, phase transformations etc [2]. in different metallic materials e.g. titanium [3], aluminum or steels and alloys [4]. In particular, the AE can be caused by stress-induced phase transformation in shape memory alloys (SMAs) [5]. AE was experimentally investigated among others in Al-Ni alloy [6], Ti-Ni alloys under load-unload [7] or cyclic tension [8] and Cu-Zn-Al [9] also in combination with calorimetric analysis in [10]. The results show that AE is a useful technique to study dynamical features of martensitic transitions, which occur through avalanches. On the other hand, the pseudoelastic deformation of the SMAs, in particular Ti-Ni, is usually macroscopically inhomogeneous due to the stress-induced phase transformation [11] and Lüders-like features can be observed [12]. It is accompanied by significant thermal effects [13] generated during nucleation and propagation of transformation fronts [14]. Thus, it is important to study local kinematic and temperature features of the tested SMAs, which can be provided by using full-field measurement techniques such as digital image correlation (DIC) and infrared thermography (IRT), respectively. Results of the thermomechanical characterization of various SMAs by these methods were reviewed in [15]. DIC was used to study tensile deformation of Ni-Ti SMA in [16] also with strain ratios analysis in [17]. Phase-transformation fronts evolution was investigated using IRT in [18] whereas development of transformation bands under selected strain rates in [19]. Combined techniques of DIC and IRT were used to study the stress-induced martensitic transformation [20] and strain rate effects [21] in Ni-Ti SMA under different deformation modes compression, compression-shear and bending.

However, in the last decades Ni-free Ti-based SMAs have been developed in order substitute Ni-Ti SMAs because Ni can cause allergies in biomedical applications [22]. In particular, Ti-Nb based SMAs have been developed [23]. The Ti-Nb SMAs can exhibit shape memory effect or superelasticity due to the stress-induced martensitic transformation from the cubic β to the orthorhombic α'' phase [24]. The addition of interstitial alloying elements, such as oxygen [25] and nitrogen [26], is known to change the stress-strain response of these SMAs [27]. This is due to the existence of lattice modulations [28], so-called nanodomains [29] or O' phase [30]. This strategy has been applied to obtain specific properties, such as nonlinear, superelastic deformation, near-zero hysteresis or invar-like behavior in oxygen [25] and nitrogen [31] added Ti-Nb based SMAs. Specifically, a class of alloys, named Gum Metals, with a typical composition Ti-23Nb-0.7Ta-2.0Zr-1.2O (at%), was developed [32]. The Ti-Nb based SMAs have been seldom studied by means of AE or DIC. Full-field analysis of the thermomechanical behavior of Gum Metal under tensile loadings using techniques of IRT [33] or coupled IRT and DIC at various strain rates [34] or under cyclic tension [35] did not present evident local effects due to high content of oxygen. However, recent systematic investigation of Ti-25Nb, Ti-25Nb-0.3O and Ti-25Nb-0.7O SMAs in tension using DIC showed that the strain fields of these alloys are inhomogeneous during the initial loading [36]. The Ti-25Nb exhibits Lüders-type deformation and the oxygen-added SMAs show different but still inhomogeneous deformation features. In view of the above, the objective of this paper was to analyze and compare AE signals generated by Ti-25Nb and Ti-25Nb-1O SMAs in the context of stress-strain curves and kinematic fields obtained using DIC during the initial load-unload tension of the specimens. The results were discussed in the light of the phase constituents of the SMAs.

2 Materials and methods

The Ti-25Nb and Ti-25Nb-1O (at%) alloys were prepared by the Ar arc melting method using pre-melted sponges of Ti (purity: >99.7%) and pure Nb (purity: 99.9%). The oxygen concentration of the Ti-25Nb-1O alloy was adjusted by amount of TiO₂ powder (purity: 99.9%). Homogeneity was ensured by repeated melting for six times and by flipping of the ingots between the melts. The ingots were sealed in a vacuumed quartz tube and homogenized at 1273 K for 120 min with subsequent air-cooling. Then the ingots were cold-rolled with a reduction in thickness of 95%. Specimens were solution-treated at 1173 K for 30 min in an Ar atmosphere, followed by water quenching. Samples for X-Ray Diffraction (XRD), Scanning Electron Microscopy (SEM) and tensile

tests were cut using an electro-discharge machine. The damaged surface was removed by chemical etching using a solution with a composition of $\text{H}_2\text{O}:\text{HNO}_3:\text{HF}=5:4:1$ by volume. SEM specimens were electropolished at 233 K using a solution of $\text{CH}_3\text{OH}:\text{C}_4\text{H}_9\text{OH}:\text{HClO}_4=10:6:1$ by volume. XRD measurements were conducted at room temperature with Cu K_α radiation using a Bruker D2 PHASER Benchtop XRD instrument. Microstructure analysis was carried out using a scanning electron microscope JEOL JSM-IT300 equipped with a EDAX-TSL electron backscatter diffraction (EBSD) system and Orientation Imaging Microscopy (OIM) analysis software. A technical drawing and a photograph of the tensile specimens are shown in Fig. 1a, b, respectively. The gauge part of each specimen was $6\text{ mm} \times 8\text{ mm} \times 0.5\text{ mm}$. The surface of the gauge part was covered with a speckle pattern for the DIC analysis. A general view of the experimental set-up is shown in Fig. 1c. Displacement-controlled load-unload tensile tests of the SMAs specimens were carried out using an Instron 5969 electromechanical testing machine at room temperature. Maximal displacement of 0.44 mm and displacement rate of $0.08\text{ mm}\cdot\text{s}^{-1}$ were used. Taking into account the specimen's geometry, an average strain rate of 10^{-2} s^{-1} was applied. The tensile deformation of the SMAs was simultaneously monitored using an AE technique and a DIC system. AE was measured using a WD differential wideband sensor, produced by Physical Acoustics Corporation which was attached to the lower grip of the testing machine using a clamp. The acoustic sensor preamplifier and amplifier had a combined gain of 60 dB and a band width of 20 to 120 kHz. The AE activity was determined using software signal post-processing procedure realized after transferring of the measured signal from the amplifier to the PC computer via Adlink USB 1901 Datalogger. Calibration of the AE registering system was performed using the Hsu-Nielsen test prior to the performed tensile deformation experiments. During the Hsu-Nielsen test, a standard and repetitive amount of AE energy was emitted. This test consisted of breaking a 0.5 mm diameter pencil lead approximately 3 mm ($\pm 0.5\text{ mm}$) from its tip by pressing it against the surface of the lower grip of testing machine. This generated an intense acoustic signal, quite similar to a natural AE sources. The applied AE signal data logger registered the invoked burst as a pulse train of amplitudes of at least 80 dB for a reference voltage of 1 mV. The synchronization between the AE signal registering system and DIC was achieved as follows: The operator of the Instron testing machine issued a signal at the beginning of the displacement of the machine traverse. At the same moment both AE acquisitions and DIC were on with the maximum uncertainty of 0.1 s. This precision level was sufficient to examine the registered data of the experiments of duration exceeding 5 s.

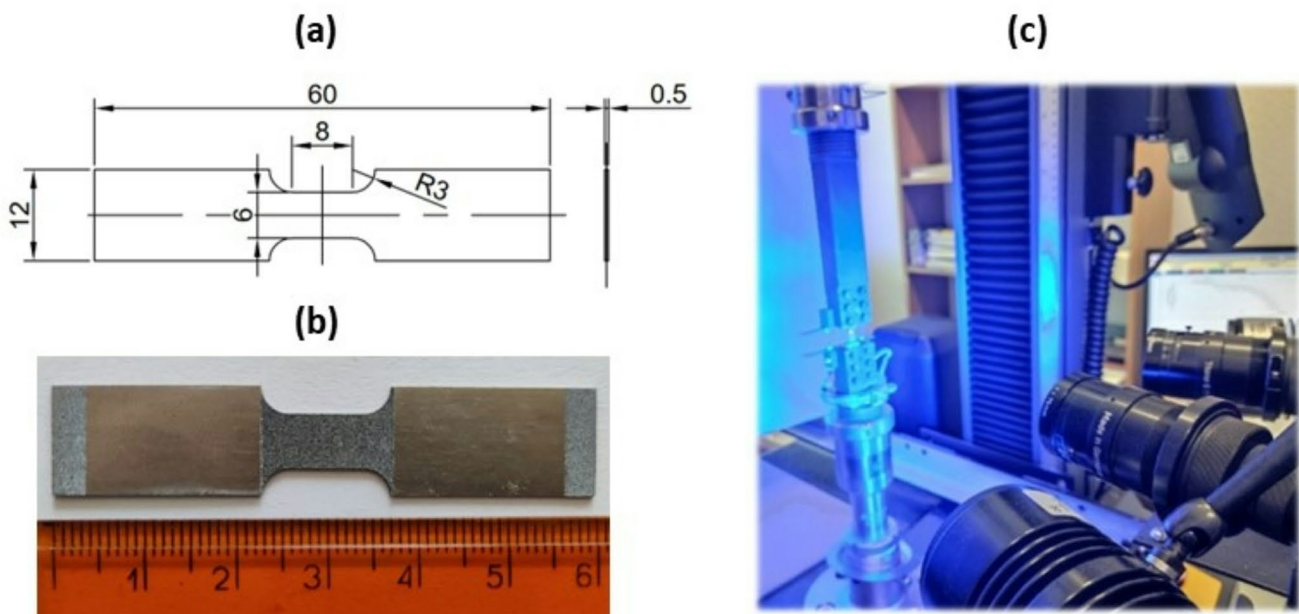


Fig. 1 a A technical drawing and b a photograph of the SMA specimen and c a general view of the experimental set-up

The DIC system ZEISS Aramis 12 M was equipped with two 12 MP cameras. Kinematic fields were generated using around 14,700 measuring points. The recording frequency was 10 Hz. The image size was 4096 px x 3000 px. The calibration deviation was 0.041 px. The measure volume was 35 mm x 25 mm x 40 mm. A function of virtual extensometer with an initial length of 8 mm was used to plot stress–strain curves.

3 Results and discussion

3.1 Phase constituents and microstructure of as-fabricated Ti–25Nb and Ti–25Nb–1O SMAs

XRD profiles of as-fabricated Ti–25Nb and Ti–25Nb–1O SMAs are presented in Fig. 2a, b, respectively. The diffraction peaks identified in the as-fabricated state of Ti–25Nb SMA correspond to the orthorhombic α'' phase and the body-centered cubic (bcc) β phase. In the case of the as-fabricated Ti–25Nb–1O SMA the diffraction peaks correspond to the β phase.

SEM images of the Ti–25Nb and Ti–25Nb–1O SMAs observed at magnifications x200 and x500 are shown in Fig. 3a–d, respectively.

The needle-like microstructure of the orthorhombic α'' martensite distributed inside β grains can be seen only in the case of the Ti–25Nb. The microstructure of the Ti–25Nb–1O SMA shows β grains.

3.2 Global mechanical behavior and AE of the Ti–25Nb and Ti–25Nb–1O SMAs under load–unload tension

Force–displacement and stress–strain curves of Ti–25Nb and Ti–25Nb–1O SMAs under load–unload tension are presented in Fig. 4a, b, respectively. The effect of 1 at% oxygen addition on the mechanical behavior of Ti–25Nb alloy is apparent. The Ti–25Nb SMA is known to exhibit shape memory effect [27]. After reaching the transformation stress, the tensile deformation of the Ti–25Nb SMA is governed by a stress-induced martensitic transformation from the cubic β phase to the orthorhombic α'' phase. After heating, the recovery strain is around 1% [24]. The Ti–25Nb–1O SMA exhibits superelasticity and the deformation mechanism is different [27]. The addition of 1 at% of oxygen results in an increased apparent yield stress and a nonlinear superelastic behavior with a significantly reduced hysteresis. The recoverable strain determined based on the stress–strain curve is around 1.5%. Although the maximum crosshead displacement was the same for Ti–25Nb and Ti–25Nb–1O SMAs, the maximum true strain determined using virtual extensometer is different, as presented in Figure 4a, b, respectively. It indicates that the deformation of the SMAs observed using DIC must be inhomogeneous and Ti–25Nb–1O SMAs under load–unload tension.

Fig. 2 XRD profiles of as-fabricated **a** Ti–25Nb and **b** Ti–25Nb–1O SMAs

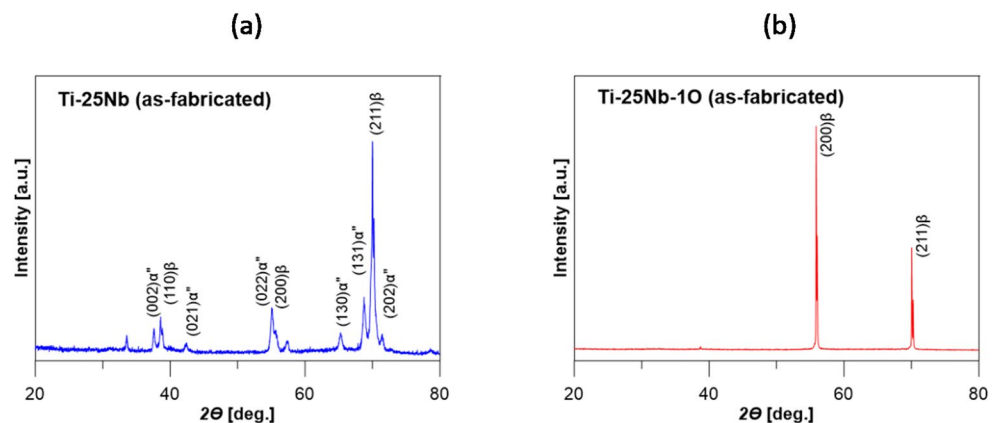


Fig. 3 SEM images of as-fabricated **a, b** Ti-25Nb and **c, d** Ti-25Nb-1O SMAs

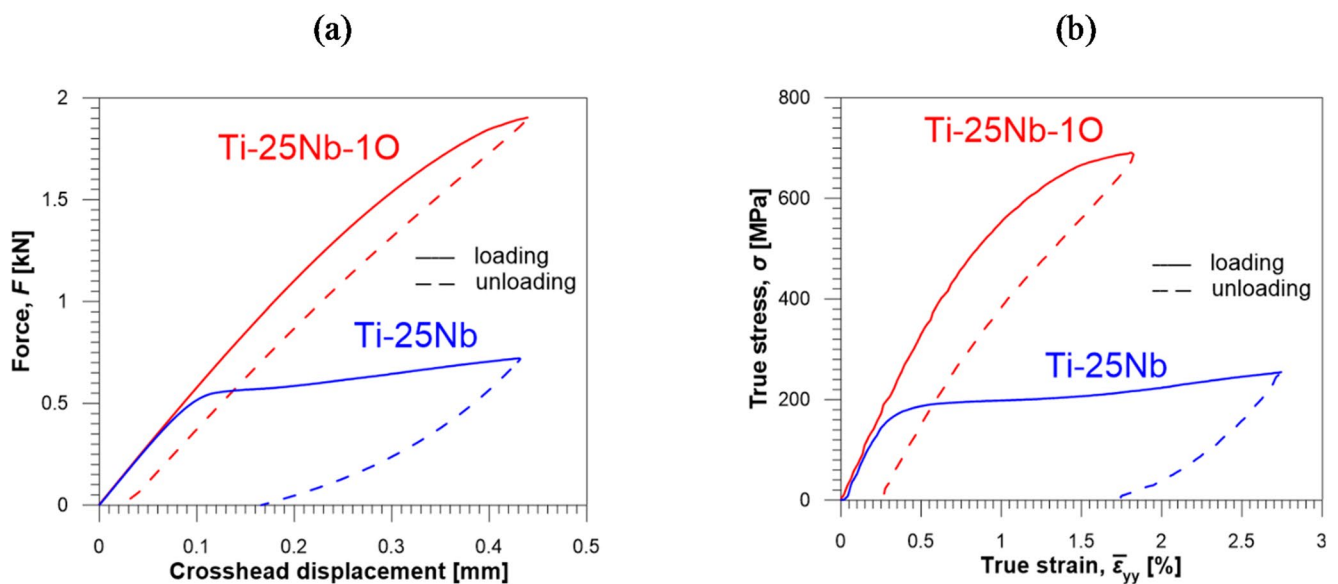
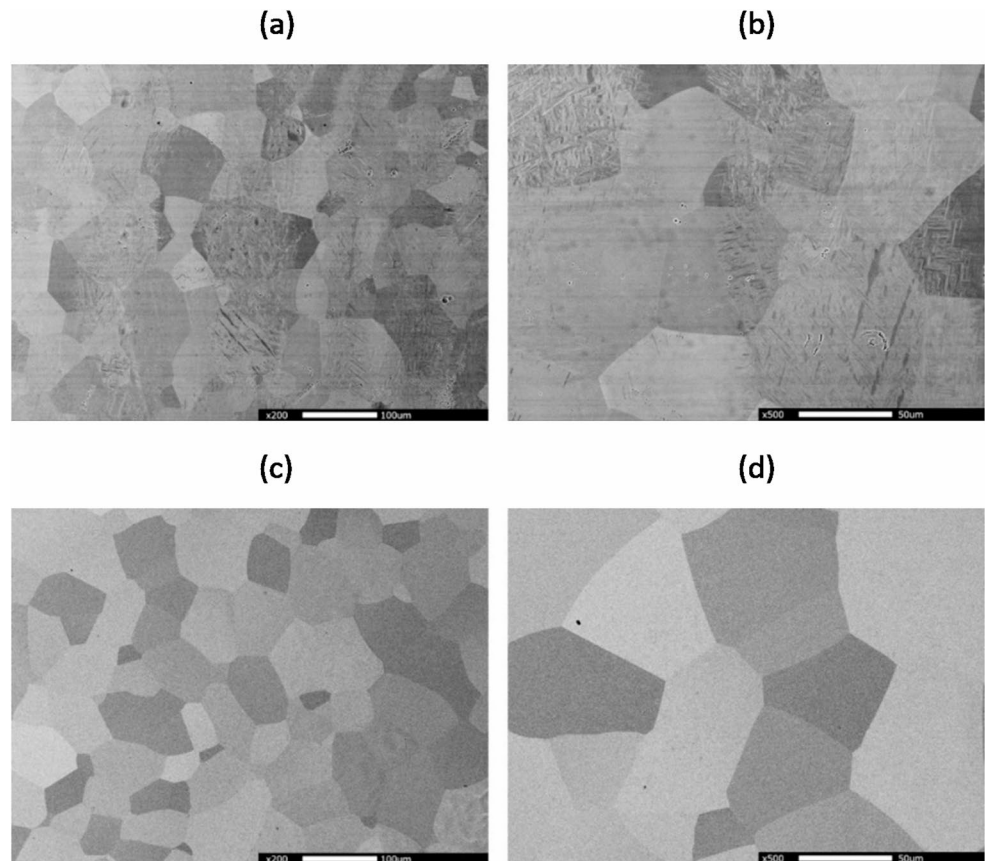


Fig. 4 **a** force-displacement curves and **b** stress-strain curves of Ti-25Nb

Stress and AE events rate vs. time curves of Ti–25Nb and Ti–25Nb–1O SMAs under load–unload tension are shown in Fig. 5a, b, respectively. The difference between the deformation mechanisms and the resulting mechanical behaviors of the SMAs was clearly reflected in the recorded AE signals. The AE events rate measured at specific stages of tensile loading of the Ti–25Nb SMA was significantly lower, than that of the Ti–25Nb–1O SMA. The true elastic deformation did not generate AE either during loading or unloading of the SMAs.

It was found that the AE activity was registered after the onset of the stress–induced phase transformations in the SMAs; in the case of the Ti–25Nb SMA after reaching the transformation stress and in the case of the Ti–25Nb–1O SMA, after reaching the nonlinear regime of deformation. The AE events rate was increasing with further tensile loading of the SMAs.

3.3 Full-field deformation of Ti–25Nb and Ti–25Nb–1O SMAs under load–unload tension in the context of the AE signal and the deformation mechanisms of the SMAs

Strain ϵ_{yy} and strain rate $\dot{\epsilon}_{yy}$ fields, where y is the direction of loading, of Ti–25Nb and Ti–25Nb–1O SMAs under load–unload tension at selected stages of the load–unload tension are presented in Fig. 6a, b, respectively. Specific stages of the SMAs loading and unloading, marked in the stress–strain curves, were selected for the analysis of the full-field deformation. In the case of the Ti–25Nb SMA the stages (A)–(I) correspond to the following values of $\bar{\epsilon}_{yy}$.

- (A) $\bar{\epsilon}_{yy} = 0.3\%$ (during loading)
- (B) $\bar{\epsilon}_{yy} = 0.5\%$ (during loading)
- (C) $\bar{\epsilon}_{yy} = 1.0\%$ (during loading)
- (D) $\bar{\epsilon}_{yy} = 1.5\%$ (during loading)
- (E) $\bar{\epsilon}_{yy} = \bar{\epsilon}_{\max}$ (maximal strain during loading)
- (F) $\bar{\epsilon}_{yy} = 2.5\%$ (during unloading)
- (G) $\bar{\epsilon}_{yy} = 2.25\%$ (during unloading)
- (H) $\bar{\epsilon}_{yy} = 2.0\%$ (during unloading)

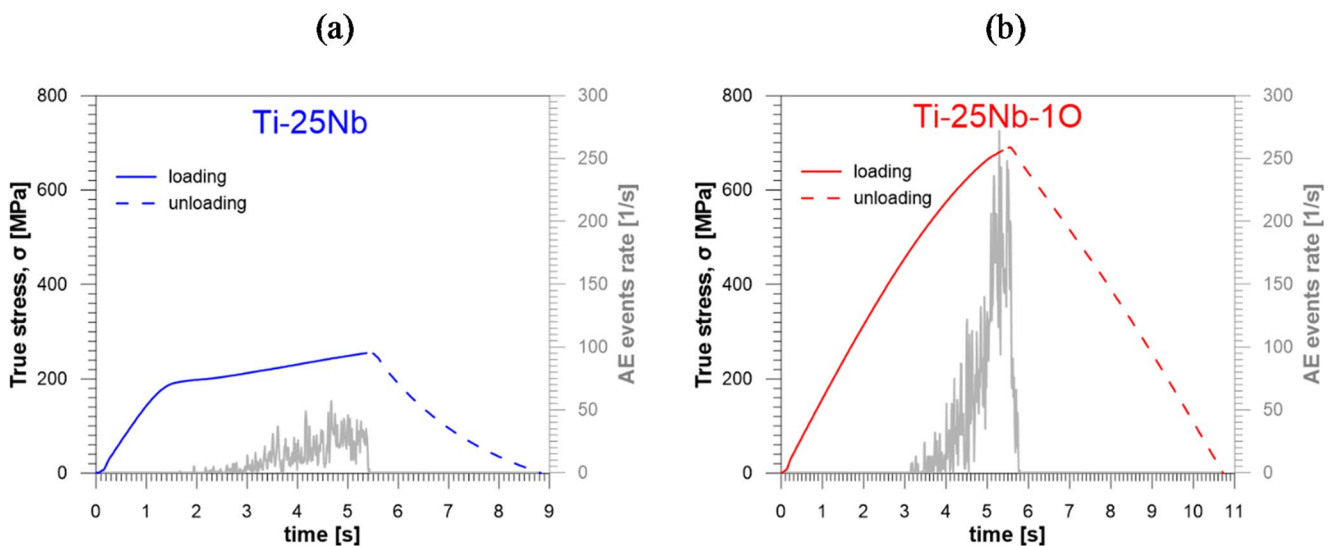
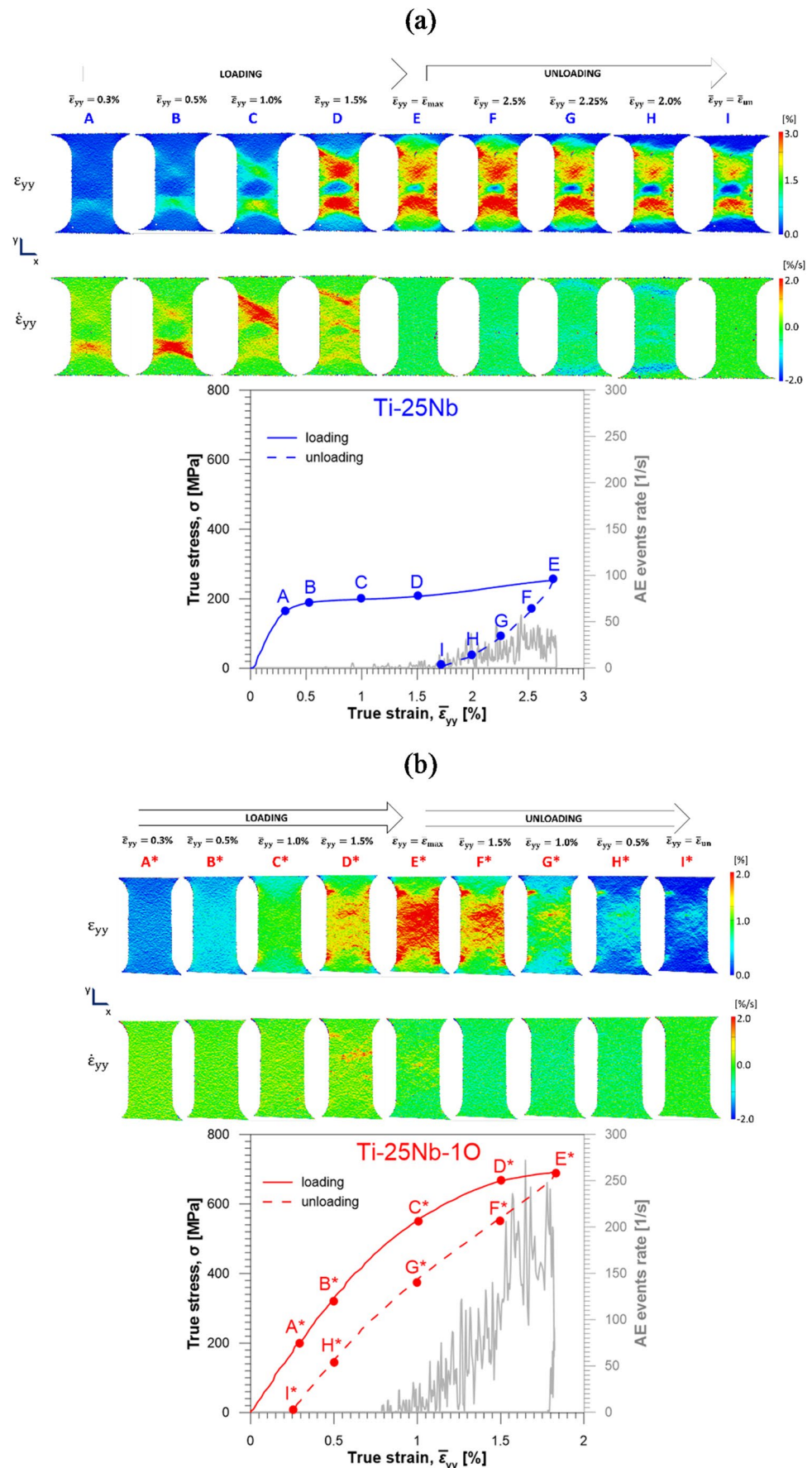


Fig. 5 Stress and AE events rate vs. time curves of **a** Ti–25Nb and **b** Ti–25Nb–1O SMAs under load–unload tension

Fig. 6 Strain ϵ_{yy} and strain rate $\dot{\epsilon}_{yy}$ fields of **a** Ti-25Nb and **b** Ti-25Nb-10 SMAs under load-unload tension at selected stages of the load-unload tension marked in stress and AE events rate versus strain curves



$$(I) \bar{\epsilon}_{yy} = \bar{\epsilon}_{un} \quad (\text{strain remaining after unloading})$$

In the case of the Ti–25Nb–10 SMA the stages (A*) – (I*) correspond to the following values of $\bar{\epsilon}_{yy}$.

$$\begin{aligned} (A^*) \quad \bar{\epsilon}_{yy} &= 0.3 \% && (\text{during loading}) \\ (B) \quad \bar{\epsilon}_{yy} &= 0.5 \% && (\text{during loading}) \\ (C^*) \quad \bar{\epsilon}_{yy} &= 1.0 \% && (\text{during loading}) \\ (D^*) \quad \bar{\epsilon}_{yy} &= 1.5 \% && (\text{during loading}) \\ (E^*) \quad \bar{\epsilon}_{yy} &= \bar{\epsilon}_{\max} && (\text{maximal strain during loading}) \\ (F^*) \quad \bar{\epsilon}_{yy} &= 1.5 \% && (\text{during unloading}) \\ (G^*) \quad \bar{\epsilon}_{yy} &= 1.0 \% && (\text{during unloading}) \\ (H^*) \quad \bar{\epsilon}_{yy} &= 0.5 \% && (\text{during unloading}) \\ (I^*) \quad \bar{\epsilon}_{yy} &= \bar{\epsilon}_{un} && (\text{strain remaining after unloading}) \end{aligned}$$

The ϵ_{yy} and $\bar{\epsilon}_{yy}$ fields of the Ti–25Nb and the Ti–25Nb–10 SMA, presented in Fig. 6a, b, show that the local deformation of the SMAs proceeds in a different manner. The Ti–25Nb exhibits a Lüders-type deformation. At the beginning of the loading process (A)–(B), the first band starts to develop in the lower part of the gauge area. During the subsequent loading (C)–(E), the strain increases and develops in the upper part of the gauge area. The unloading of the Ti–25Nb SMA (E) – (I), reduces the strain in the upper part of the gauge area. After unloading (I), the strain remains concentrated in a form of two major bands.

The deformation of the Ti–25Nb–10 SMA shows distinct but still localized features. At the beginning of the loading process (A*) – (B*), strain ϵ_{yy} fields look rather homogenous. However, further loading (C*) – (E*) exhibits some inhomogenous features. In particular, the kinematic fields captured in (D*) reveal few areas with increased strain, whereas those captured in (E*) look definitely more homogenous. During the unloading (E*) – (I*), the strain is gradually reduced. The kinematic fields captured in (G*) show again some areas with higher strain. After unloading (I*), the remaining strain concentrates in the corners and in the central part of the gauge area.

XRD profiles of the Ti–25Nb and Ti–25Nb–10 SMAs in the as-fabricated state and after unloading determined for $69^\circ < 2\theta < 72^\circ$ are shown in Fig. 7a, b, respectively. In the case of the Ti–25Nb SMA, the content of orthorhombic α'' martensite increased after unloading. However, in the case of the Ti–25Nb–10 SMA no peaks corresponding to the orthorhombic α'' martensite were identified either in the as-fabricated state or after unloading.

SEM images of the Ti–25Nb SMA after unloading with magnifications x1,000 and x2,000 are shown in Figs. 8a, b, respectively. The stress-induced α'' martensites are clearly observed in the micrographs. Two types of martensite variants induced in various grains can be found.

EBSD orientation maps of the Ti–25Nb SMA after unloading obtained with respect to rolling direction (RD), transverse direction (TD) and normal direction (ND) are presented in Figs. 9a–c, respectively. Point-to-origin misorientation profiles along A–A and B–B lines marked in the EBSD orientation map obtained with respect to RD (Fig. 9c) are shown in Figs. 9d.

Deformation twins with misorientation of 50 deg, typical for the β -Ti alloys, are observed. The spatial resolution of the EBSD measurements was probably too low to detect α'' martensites seen in SEM images, presented in Figs. 8a, b.

SEM picture of the Ti–25Nb–10 SMA after unloading with magnification x200 is shown in Fig. 10a. EBSD orientation maps of the Ti–25Nb–10 SMA after unloading obtained with respect to RD, TD and ND are presented in Figs. 10b–d, respectively. No obvious deformation twins were found either in the SEM image or EBSD maps.

The obtained XRD profiles show that the deformation mechanisms of the alloys are different. Lüders-type deformation and a relatively low AE signal obtained for the Ti–25Nb SMA are mainly associated with the

Fig. 7 XRD profiles of Ti–25Nb and Ti–25Nb–1O SMAs **a** in the as-fabricated state and **b** after unloading

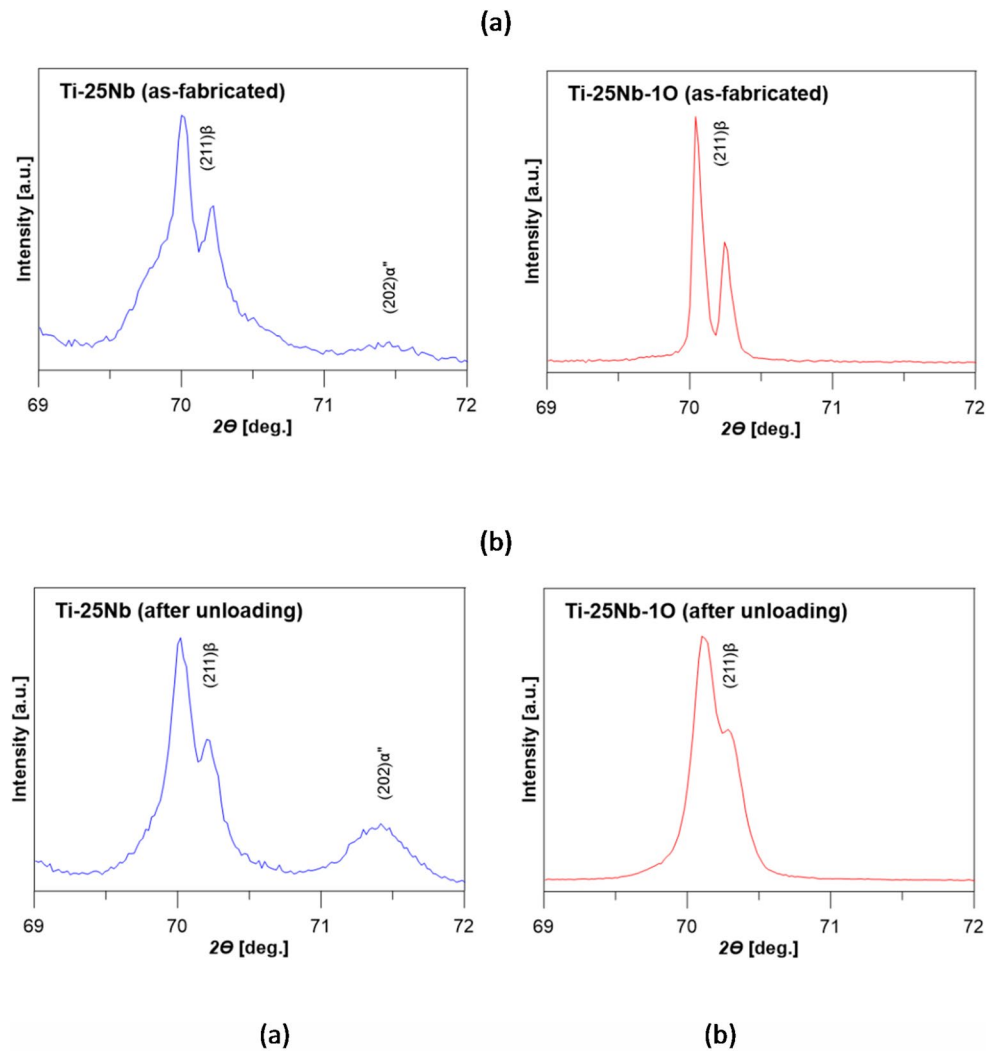
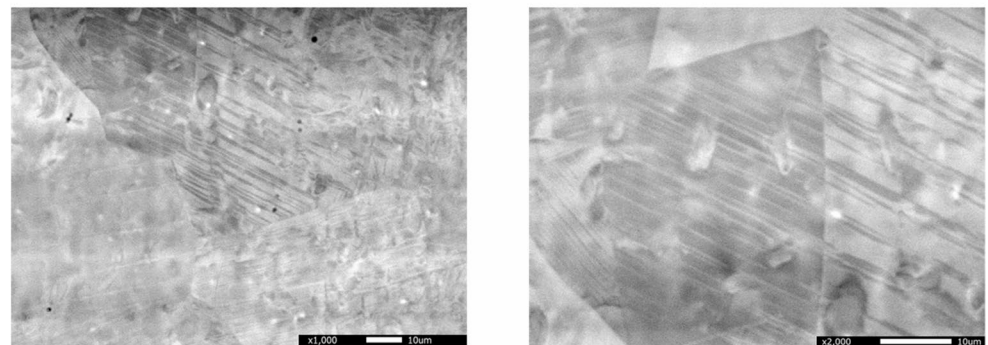


Fig. 8 SEM images of the Ti–25Nb SMA after unloading with magnifications. **a** x1,000 and **b** x2,000



first-order martensitic transformation from the β phase to the orthorhombic α'' martensite. Two variants of the latter were observed in Fig. 8a, b. $\{332\}$ (113) twinning also occurs in this alloy, as shown in Fig. 9a–d, due to the instability of the β phase [37, 38]. However, its contribution to the measured acoustic effects should be rather low in the initial stage of tension. The Ti–25Nb–1O SMA under tensile loading generates stronger AE signal and exhibits different but still inhomogeneous deformation. The nonlinear superelastic deformation of the Ti–25Nb–1O SMA is due to the second-order phase transformation, as it was suggested in [28]. Based on the in-situ XRD measurement during tensile loading, it was detected that the β phase peak shifted continuously to the higher angle

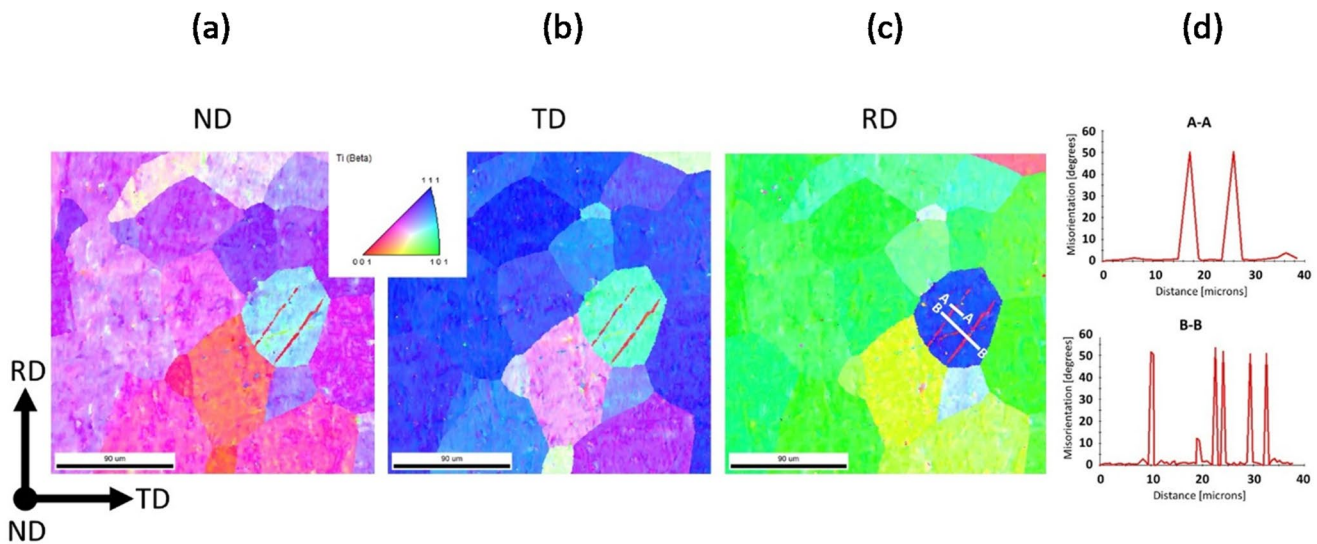


Fig. 9 EBSD orientation maps of the Ti–25Nb SMA after unloading obtained with respect to: **a** RD, **b** TD and **c** ND, **d** point-to-origin misorientation profiles along A-A and B-B lines marked in the EBSD orientation map obtained with respect to RD

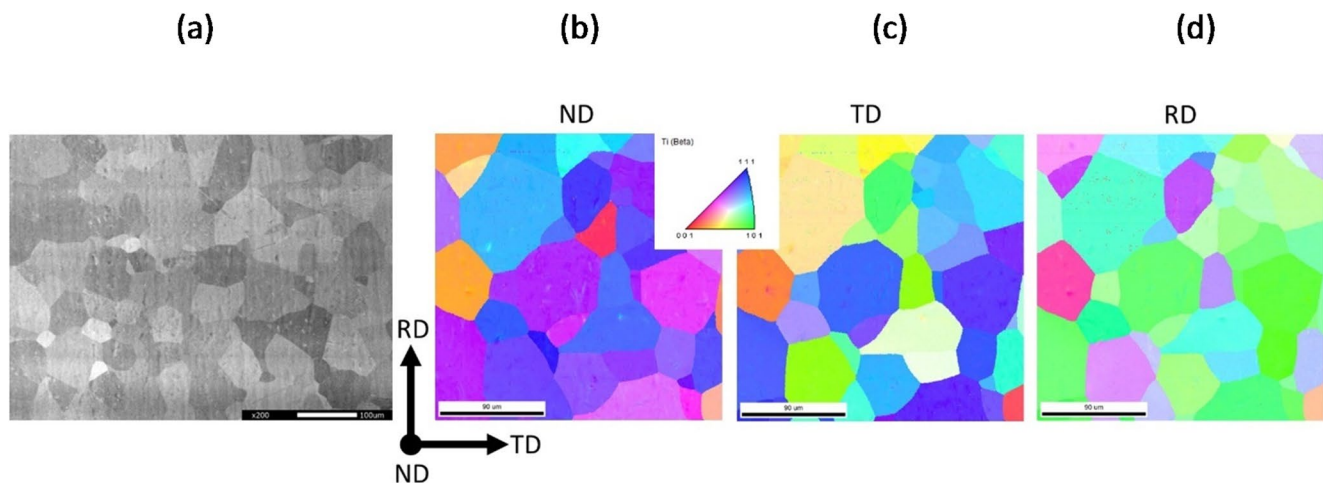


Fig. 10 **a** SEM picture and EBSD orientation maps of the Ti–25Nb–1O SMA after unloading obtained with respect to: **b** ND, **c** TD and **d** RD

position. The final stage of loading of the Ti–25Nb–1O SMA is accompanied by the strongest AE activity due to the onset of plastic deformation. The addition of oxygen stabilizes the β phase in the Ti–25Nb–1O SMA and can suppress the $\{332\} \langle 113 \rangle$ twinning until certain extend. In fact, no apparent deformation twins were found either in the SEM image or EBSD maps presented in Fig. 10a–d. However, other mechanisms of plastic deformation can be also involved at this stage of loading [37, 38].

4 Conclusions

The Ti–25Nb and Ti–25Nb–1O SMAs under load–unload tension were monitored by combined techniques of AE and DIC in the initial stage of tensile deformation. The following conclusions can be drawn:

- (1) The AE was confirmed to be an effective method for tracking the stress-induced phase transformation of the Ti–25Nb and Ti–25Nb–10 SMA under loading.
- (2) The effect of the 1 at% of oxygen addition to Ti–25Nb had a significant influence on the AE, namely the number of AE events rate was significantly lower in the case of the Ti–25Nb SMA comparing to that of the Ti–25Nb–10 SMA.
- (3) The kinematic fields determined using DIC showed that the deformation of the studied SMAs proceeds in a different way. On the one hand the Ti–25Nb SMA exhibited.
- (4) a Lüders-type deformation with macroscopically captured martensitic bands. On the other hand, the Ti–25Nb–10 SMA deformed in a distinct but still inhomogeneous manner.
- (5) The experimental findings are directly related to the differences in the deformation mechanisms. The analysis of the phase constituents and microstructures of the SMAs showed an increased content of the orthorhombic α'' martensite and deformation twinning only in the Ti–25Nb SMA after unloading.

Acknowledgements Karol M. Golański acknowledges the support of the Japan Society for the Promotion of Science (JSPS) Postdoctoral Fellowship (ID No. P20812). The authors would like to express their gratitude to Mr. Leszek Urbański from the Institute of Fundamental Technological Research, Polish Academy of Sciences for conducting tensile tests and his diligent efforts in data collection as well as processing.

Data availability The data that support the findings of this study are available on request from the corresponding author.

Declarations

Conflict of interest The authors declare that they have no known competing financial interests or personal relationships that could have appeared to influence the work reported in this paper.

Open Access This article is licensed under a Creative Commons Attribution 4.0 International License, which permits use, sharing, adaptation, distribution and reproduction in any medium or format, as long as you give appropriate credit to the original author(s) and the source, provide a link to the Creative Commons licence, and indicate if changes were made. The images or other third party material in this article are included in the article's Creative Commons licence, unless indicated otherwise in a credit line to the material. If material is not included in the article's Creative Commons licence and your intended use is not permitted by statutory regulation or exceeds the permitted use, you will need to obtain permission directly from the copyright holder. To view a copy of this licence, visit <http://creativecommons.org/licenses/by/4.0/>.

References


1. Ono K. Acoustic emission. In: Rossing TD, editor. Springer handbook of acoustics. New York: Springer; 2014. pp. 1209–27.
2. McCrory JP, Vinogradov A, Pearson MR, Pullin R, Holford KM. Acoustic emission monitoring of metals. In: Grosse CU, Ohtsu M, Aggelis DG, Shiotani T, editors. Acoustic emission testing. Springer Tracts in Civil Engineering. Cham: Springer; 2022. pp. 529–65.
3. Friesel M, Carpenter SH. Determination of the sources of acoustic emission generated during the deformation of titanium. Metall Trans A. 1984. <https://doi.org/10.1007/BF02664898>.
4. Wadley HNG, Mehrabian R. Acoustic emission for materials processing: a review. Mater Sci Eng. 1984. [https://doi.org/10.1016/0025-5416\(84\)90086-7](https://doi.org/10.1016/0025-5416(84)90086-7).
5. Planes A, Mañosa L, Vives E. Acoustic emission in martensitic transformations. J Alloys Compd. 2013. <https://doi.org/10.1016/j.jallcom.2011.10.082>.
6. Baram J, Rosen M. Some observations on acoustic emission generated during thermoelastic phase transformation in Al–Ni and Ti–Ni alloys. Scr Mater. 1979. [https://doi.org/10.1016/0036-9748\(79\)90109-1](https://doi.org/10.1016/0036-9748(79)90109-1).
7. Pieczyńska EA, Tobushi H, Takeda K, Stróż D, Ranachowski Z, Kulasiński K, Kúdela S Jr, Luckner J. Martensite transformation bands studied in TiNi shape memory alloy by infrared and acoustic emission techniques. Kovove Mater. 2012;50:309–18.

8. Nataf GF, Romanini M, Vives E, Žužek B, Planes A, Tušek J, Moya X. Suppression of acoustic emission during superelastic tensile cycling of polycrystalline Ni_{50.4}Ti_{49.6}. *Phys Rev Mater*. 2020. <https://doi.org/10.1103/PhysRevMaterials.4.093604>.
9. Amengual A, Garcias F, Marco F, Segui C, Torra V. Acoustic emission of the interface motion in the martensitic transformation of Cu-Zn-Al shape memory alloy. *Acta Metall*. 1988. [https://doi.org/10.1016/0001-6160\(88\)90332-X](https://doi.org/10.1016/0001-6160(88)90332-X).
10. Baró J, Martín-Olalla JM, Romero FJ, Gallardo MC, Salje EKH, Vives E, Planes A. Avalanche correlations in the martensitic transition of a Cu–Zn–Al shape memory alloy: analysis of acoustic emission and calorimetry. *J Condens Matter Phys*. 2014. <https://doi.org/10.1088/0953-8984/26/12/125401>.
11. Miyazaki S, Otsuka K, Suzuki Y. Transformation pseudoelasticity and deformation behavior in a Ti-50.6at%Ni alloy. *Scr Mater*. 1981. [https://doi.org/10.1016/0036-9748\(81\)90346-X](https://doi.org/10.1016/0036-9748(81)90346-X).
12. Miyazaki S, Imai T, Otsuka K, Suzuki Y. Lüders-like deformation observed in the transformation pseudoelasticity of a Ti-Ni alloy. *Scr Mater*. 1981. [https://doi.org/10.1016/0036-9748\(81\)90265-9](https://doi.org/10.1016/0036-9748(81)90265-9).
13. Shaw JA, Kyriakides S. Thermomechanical aspects of NiTi. *J Mech Phys Solids*. 1995. [https://doi.org/10.1016/0022-5096\(95\)00024-D](https://doi.org/10.1016/0022-5096(95)00024-D).
14. Shaw JA, Kyriakides S. On the nucleation and propagation of phase transformation fronts in a NiTi alloy. *Acta Mater*. 1997. [https://doi.org/10.1016/S1359-6454\(96\)00189-9](https://doi.org/10.1016/S1359-6454(96)00189-9).
15. Delpueyo S, Jury A, Balandraud X, Grédiac M. Applying Full-Field measurement techniques for the thermomechanical characterization of shape memory alloys: A review and classification. *Shap Mem Superelasticity*. 2021. <https://doi.org/10.1007/s40830-021-00355-w>.
16. Daly S, Ravichandran G, Bhattacharya K. Stress-induced martensitic phase transformation in thin sheets of nitinol. *Acta Mater*. 2007. <https://doi.org/10.1016/j.actamat.2007.02.011>.
17. Bewerse C, Gall KR, McFarland GJ, Zhu P, Brinson LC. Local and global strains and strain ratios in shape memory alloys using digital image correlation. *Mater Sci Eng A*. 2013. <https://doi.org/10.1016/j.msea.2013.01.030>.
18. Pieczyska EA, Gadaj SP, Nowacki WK, Tobushi H. Phase-Transformation fronts evolution for Stress- and Strain-Controlled tension tests in TiNi shape memory alloy. *Exp Mech*. 2006. <https://doi.org/10.1007/s11340-006-8351-y>.
19. Pieczyska EA, Tobushi H, Kulasinski K. Development of transformation bands in TiNi SMA for various stress and strain rates studied by a fast and sensitive infrared camera. *Smart Mater Struct*. 2013. <https://doi.org/10.1088/0964-1726/22/3/035007>.
20. Elibol C, Wagner MFX. Investigation of the stress-induced martensitic transformation in pseudoelastic NiTi under uniaxial tension, compression and compression–shear. *Mater Sci Eng A*. 2015. <https://doi.org/10.1016/j.msea.2014.10.054>.
21. Elibol C, Wagner MFX. Strain rate effects on the localization of the stress-induced martensitic transformation in pseudoelastic NiTi under uniaxial tension, compression and compression–shear. *Mater Sci Eng A*. 2015. <https://doi.org/10.1016/j.msea.2015.07.039>.
22. Miyazaki S, Kim HY, Hosoda H. Development and characterization of Ni-free Ti-base shape memory and superelastic alloys. *Mater Sci Eng A*. 2006. <https://doi.org/10.1016/j.msea.2006.02.054>.
23. Kim HY, Miyazaki S. Several issues in the development of Ti–Nb–Based shape memory alloys. *Shape Mem Superelasticity*. 2016. <https://doi.org/10.1007/s40830-016-0087-7>.
24. Kim HY, Ikehara Y, Kim JI, Hosoda H, Miyazaki S. Martensitic transformation, shape memory effect and superelasticity of Ti–Nb binary alloys. *Acta Mater*. 2006. <https://doi.org/10.1016/j.actamat.2006.01.019>.
26. Tahara M, Kim HY, Inamura T, Hosoda H, Miyazaki S. Role of interstitial atoms in the microstructure and non-linear elastic deformation behavior of Ti–Nb alloy. *J Alloys Compd*. 2013. <https://doi.org/10.1016/j.jallcom.2011.12.113>.
26. Tahara M, Kim HY, Hosoda H, Miyazaki S. Shape memory effect and Cyclic deformation behavior of Ti–Nb–N alloys. *Funct Mater Lett*. 2009;2:2, 79–82.
27. Miyazaki S. My experience with Ti–Ni–Based and Ti–Based shape memory alloys. *Shap Mem Superelasticity*. 2017. <https://doi.org/10.1007/s40830-017-0122-3>.
28. Tahara M, Kim HY, Inamura T, Hosoda H, Miyazaki S. Lattice modulation and superelasticity in oxygen-added β-Ti alloys. *Acta Mater*. 2011. <https://doi.org/10.1016/j.actamat.2011.06.015>.
29. Wei LS, Kim HY, Miyazaki S. Effects of oxygen concentration and phase stability on nano-domain structure and thermal expansion behavior of Ti–Nb–Zr–Ta–O alloys. *Acta Mater*. 2015. <https://doi.org/10.1016/j.actamat.2015.08.054>.
30. Gao Y, Chen J, Gan Y, Liang X, Chen H, Zeng D, Yang C, Jiang W, Ma C, Xiao W. Biomedical Ti–Nb–O alloy with high strength and ultra-low young's modulus. *Mater Res Lett*. 2024. <https://doi.org/10.1080/21663831.2024.2437402>.
31. Fu J, Kim HY, Miyazaki S. Effect of N addition on nano-domain structure and mechanical properties of a meta-stable Ti–Zr based alloy. *Scr Mater*. 2021. <https://doi.org/10.1016/j.scriptamat.2021.114068>.
32. Saito T, Furuta T, Hwang JH, Kuramoto S, Nishino K, Suzuki N, Chen R, Yamada A, Ito K, Seno Y, Nonaka T, Ikehata H, Nagasako N, Iwamoto C, Ikuhara Y, Sakuma T. *Science*. 2003. <https://doi.org/10.1126/science.1081957>.
33. Golasiński KM, Pieczyska EA, Staszczak M, Maj M, Furuta T, Kuramoto S. Infrared thermography applied for experimental investigation of thermomechanical couplings in gum metal. *Quant InfraRed Thermogr J*. 2017. <https://doi.org/10.1080/17686733.2017.1284295>.

34. Pieczyska EA, Maj M, Golasiński KM, Staszczak M, Furuta T, Kuramoto S. Thermomechanical studies of yielding and strain localization phenomena of gum metal under tension. *Materials*. 2018. <https://doi.org/10.3390/ma11040567>.
35. Golasiński KM, Maj M, Urbański L, Staszczak M, Gradys A, Pieczyska EA. Experimental study of thermomechanical behaviour of gum metal during Cyclic tensile loadings: the quantitative contribution of IRT and DIC. *Quant InfraRed Thermogr J*. 2023. <https://doi.org/10.1080/17686733.2023.2205762>.
36. Golasiński K, Maj M, Tasaki W, Pieczyska EA, Kim HY. Full-Field deformation study of Ti–25Nb, Ti–25Nb–0.3O and Ti–25Nb–0.7O shape memory alloys during tension using digital image correlation. *Metall Mater Trans - Phys Metall*. 2024. <https://doi.org/10.1007/s11661-024-07414-8>.
37. Hanada S, Ozeki M, Izumi O. Deformation characteristics in β phase Ti-Nb alloys. *Metall Mater Trans - Phys Metall*. 1985. <https://doi.org/10.1007/BF02814829>.
38. Li X, Zhang Z, Wang J. Deformation twinning in body-centered cubic metals and alloys. *Prog Mater Sci*. 2023. <https://doi.org/10.1016/j.pmatsci.2023.101160>.

Publisher's note Springer Nature remains neutral with regard to jurisdictional claims in published maps and institutional affiliations.

Authors and Affiliations

Karol Marek Golasiński¹  · Adam Brodecki² · Zbigniew Ranachowski² · Wataru Tasaki³ · Elżbieta Alicja Pieczyska² · Hee Young Kim³

✉ Karol Marek Golasiński
k.golasinski@uksw.edu.pl

¹ Multidisciplinary Research Center, Cardinal Stefan Wyszyński University in Warsaw, 1 Marii Konopnickiej Str., Dziekanów Leśny 05-092, Poland

² Institute of Fundamental Technological Research, Polish Academy of Sciences, 5b Adolfa Pawińskiego Str., Warsaw 02-106, Poland

³ Department of Materials Science, Institute of Pure and Applied Sciences, University of Tsukuba, Tsukuba 305-8573, Ibaraki, Japan